Phyllotactic order from radial growth of spatial symmetry-breaking instabilities in supercritical conditions

Marcello A. Budroni [*]
Department of Chemical, Physical, Mathematical and Physical Sciences, University of Sassari, Via Vienna, 2 - 07100 Sassari, Italy

Giulio Facchini
Université Paris Cité, CNRS, Matière et Systèmes Complexes, F-75013 Paris, France

Fabian Brau and Anne De Wit
Université libre de Bruxelles (ULB), Nonlinear Physical Chemistry Unit, CP231, 1050 Brussels, Belgium

(Received 1 June 2026; accepted 8 September 2026; published 2 October 2026)

Phyllotactic patterns, i.e., the arrangements of organs around a stem in some plants, represent not only fascinating geometries but also a source of inspiration for advanced biomimetic technological applications. Recently, spatial symmetry-breaking instabilities have been shown to feature, in some cases, phyllotactic symmetries when the radial growth of the pattern is slaved to a reactive front. We show here that phyllotactic ordering can also emerge when a homogeneous system is unstable with respect to a spatially self-organizing instability, and pattern formation is triggered by a localized perturbation that propagates radially. To do so, we numerically investigate the emergence of phyllotactic patterns from two different spatial symmetry-breaking instabilities coupled to radial growth in supercritical conditions: a far-from-equilibrium Turing instability studied here with the Brusselator model and equilibrium spinodal decomposition modeled by the Cahn-Hilliard equation. In both cases, radial expansion of the perturbations leads to the formation of concentric rings that subsequently fragment into spots, generating highly symmetric phyllotactic arrangements. The resulting patterns belong to the family of whorled modes, characterized by equal numbers of clockwise and counterclockwise parastichies. The morphologies are robust under variations of the characteristic wavelength and exhibit self-similarity when rescaled by this intrinsic length scale. A geometric analysis reveals that phyllotactic order arises from a space-optimization hexagonal lattice packing, as confirmed by Voronoi diagrams and representations in rescaled polar coordinates. Despite the common lattice structure, the two instabilities may select different orientations of propagation with respect to the radial direction. These results confirm the radial growth of spatial symmetry-breaking systems as a universal mechanism able to generate phyllotactic order.

DOI: 10.1103/njhc-tl7p

I. INTRODUCTION

From the arrangement of petals in flowers to the geometric motifs decorating the coats of animals such as tigers and zebras, nature displays an extraordinary repertoire of ordered forms. These structures exert a nearly innate attraction, evoking a sense of harmony and coherence. Neuroscientific studies support this predisposition through the Processing Fluency Theory [1], according to which the brain processes symmetric and regularly structured stimuli with reduced cognitive effort, activating positive responses linked to dopaminergic reward circuits. The appeal of ordered structures thus reflects not only esthetic preference but also deep cognitive mechanisms. It is therefore not surprising that the study of morphogenesis [2]—the set of processes guiding the development of form and structure in living organisms—and of self-organization phenomena, in general [3], has transversely attracted researchers from disciplines spanning biology, chemistry, mathematics, physics, and engineering. Of key interest is the intrinsic ability of nonintelligent systems to self-organize autonomously, generating highly complex and functionally effective structures without external control or centralized coordination. As an example, reaction-diffusion systems are known to provide various pattern forming instabilities that play a pivotal role in biological and physicochemical systems [4].

One of the most intriguing examples of biological self-organization is phyllotaxis [5,6], namely, the ordered geometric arrangement of leaves, petals, or botanical seeds around a stem. Phyllotactic patterns display remarkable mathematical regularities, connected in some cases with the Fibonacci sequence and the golden ratio. Crystallinelike phyllotactic patterns typically develop along a unique generative spiral, the so-called ontological spiral, on which successive elements are positioned, separated by a constant divergence angle Θ. Although the ontological spiral represents the underlying generative support, the visible structure is characterized by a family of counter-rotating spirals (parastichies), with n spirals

[*]Contact author: mabudroni@uniss.it

 ©2026 American Physical Society

turning in one direction and m other spirals in the opposite direction.

Strikingly, the most common arrangements found in nature exhibit a divergence angle close to the golden section, $\Theta = 2\pi(1-\tau)$, with $\tau = (\sqrt{5}-1)/2$ (i.e. $\Theta \approx 137.5^\circ$ or 2.4 rad) and parastichy numbers (n, m) corresponding to consecutive terms of the Fibonacci series $F_l = 1, 1, 2, 3, 5, 8, 13, 21, 34, \ldots$, in which each term equals the sum of the two preceding ones [7]. In classical phyllotaxy, if the points of the pattern are indexed in order of increasing radius, a parastichy of order n connects the points l, $l+n$, $l+2n$, ... that are successively separated by an angular increment $n\Theta \pmod{2\pi}$. Such an organization is not accidental but rather the result of evolutionary optimization maximizing light exposure, photosynthetic efficiency, and minimization of competition among plant organs [5,6]. In parallel, another class of phyllotactic order can emerge whenever multiple identical primordia appear simultaneously and accommodate on a growing curved front according to a criterion of maximal packing. Less abundant in botany than Fibonacci spiral modes, the resulting structures typically belong to the family of whorled modes characterized by an equal number of left- and right-turning spirals ($n \approx m$) [8].

While the geometric properties of these botanical phyllotactic families have been well understood, a fundamental question remains open: What are the minimal physical mechanisms capable of generating such patterns? A seminal step toward answering this question was provided by Douady and Couder [9], who demonstrated experimentally that phyllotactic patterns can arise from self-organization in a simple physical experiment involving repulsive ferrofluid droplets periodically released at a fixed radius, R_0, from a central source and advected radially at constant velocity, V_0, under the action of a magnetic field. The system is governed by a single dimensionless control parameter, the Richards plastochrone ratio $G = V_0 T/R_0$, where T is the release period [10]. By tuning G, different phyllotactic topologies with varying divergence angles were obtained, including the golden angle configuration commonly observed in plants. This experiment shows a robust way toward physical phyllotaxy and allows us to identify three essential ingredients for phyllotactic self-organization: (i) radial advection at constant speed, (ii) periodic central emission of identical elements, and (iii) mutual repulsion between them. Phyllotacticlike patterns have meanwhile been evidenced in other physical systems, such as in layered superconductors [11], self-assembled microstructures [12], magnetic cacti [13], optics [14], bubbles on a free surface [15], etc. In all these systems, the induction and selection of the final patterns require external control. Simulations have further shown that spiral families of spots can also be constructed behind inwardly radially moving pattern fronts, but, there again, the symmetries were then seeded in the outer boundary conditions [16].

A further conceptual advance arises from considering intrinsically self-organized systems in which spatial symmetry-breaking instabilities (such as spinodal decomposition or a reaction-diffusion Turing instability) generate finite-size localized spots [17]. In these systems, the characteristic wavelength λ selected by the instability is intrinsic to the dynamics and is not imposed externally. This wavelength defines both an optimal interspot distance and a characteristic timescale $\tau = \lambda^2/D$, where D is the relevant diffusion coefficient. These intrinsic spatial and temporal scales can effectively reproduce the role played by repulsion and periodic release in the ferrofluid experiment [9], but without external forcing or control. Numerical simulations of the Cahn-Hilliard (CH) model (describing phase separation) and of reaction–diffusion Turing patterns, as well as experimental precipitation patterns, have shown that phyllotactic morphologies spontaneously emerge when the symmetry-breaking instability is slaved to a radially growing chemical front [17]. Despite the different physical origins of the instability, the resulting structures share key features: they display local hexagonal packing, corresponding to one of the most stable pavements of the 2D plane [18]. Moreover, they belong to the family of whorled modes shown to develop when several disks of radius λ appear at once at a growing front and must accommodate onto a curved front of length L [8]. The useful control parameter is then the geometric factor $\Gamma = \lambda/L$, and symmetric ($n = m$) patterns are favored [19].

In this context, our objective is to extend and generalize the framework of phyllotacticlike symmetries growing in self-organized systems characterized by spatial symmetry-breaking instabilities with an intrinsic wavelength. Instead of slaving the radial growth of a spotted pattern to a chemical front [17], we show, through numerical simulations, that phyllotactic patterns can also simply emerge when a spatial symmetry breaking instability develops following the outward radial propagation of a localized perturbation in an unstable medium under supercritical conditions. To substantiate the generality of the proposed mechanism, we consider two conceptually distinct sources of instability: first, the Turing instability, paradigmatic of far-from-equilibrium self-organization; and, second, spinodal decomposition described by the Cahn–Hilliard model, representative of equilibrium thermodynamic phase separation.

II. TURING SPOTS

A. Brusselator model

As a first case, we consider the perturbation-driven radial growth of a Turing instability for values of parameters featuring spots. To do so, we use the Brusselator, a classical kinetic model used to describe oscillations and pattern formation in spatially extended systems far from equilibrium [3,18,20,21]. The advantages of the Brusselator are that (i) it depends on a minimum set of parameters, (ii) it can feature both Turing spots and stripes, and (iii) it is simple enough to perform an analytical characterization. The kinetic scheme of the irreversible Brusselator model reads

$$\begin{aligned} \mathrm{A} &\to \mathrm{X}, \\ \mathrm{B} + \mathrm{X} &\to \mathrm{Y} + \mathrm{D}, \\ 2\mathrm{X} + \mathrm{Y} &\to 3\mathrm{X}, \\ \mathrm{X} &\to \mathrm{E}, \end{aligned} \tag{1}$$

where $\{A, B\}$ are the initial reactants and $\{X, Y\}$ are the reaction intermediates, featuring the autocatalytic X and the inhibitor Y species, respectively. In the pool chemical

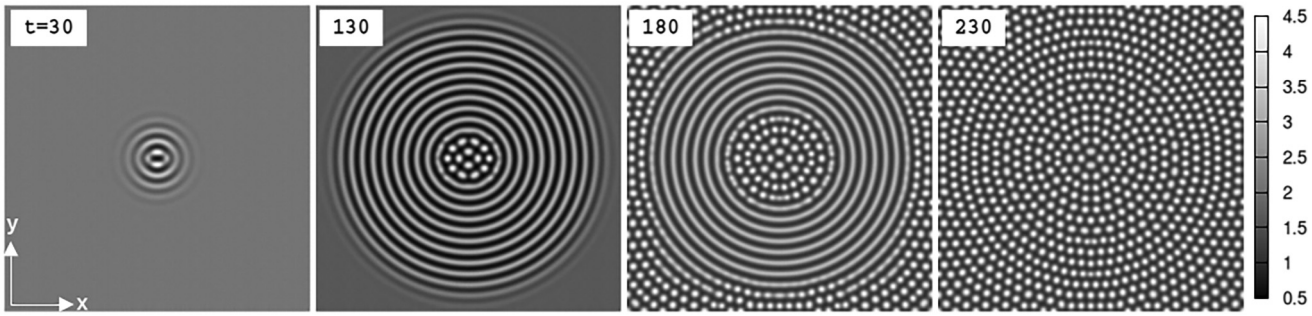

FIG. 1. Spatiotemporal evolution of the concentration of species $Y(x, y)$ obtained by simulating the Brusselator model (2) with $A_0 = 2$, $B_0 = 3$, $D_X = 3$, $\delta = 10$, $L = 380$. The Turing pattern invades the unstable steady state radially starting from a central localized perturbation. The dimensionless time is given in the upper left corner.

approximation [3], we assume that the reactants A and B are homogeneously distributed and in sufficient excess such that their concentrations can be considered constant. This is physically consistent with some batch nonlinear chemical oscillators like the Belousov-Zhabotinsky reaction [22]. The reaction-diffusion equations for the intermediates X and Y read [23,24]

$$\partial_t X = D_X \nabla^2 X + A - (B+1)X + X^2 Y, \tag{2a}$$

$$\partial_t Y = D_Y \nabla^2 Y + BX - X^2 Y, \tag{2b}$$

where D_X and D_Y are the diffusion coefficients of X and Y, respectively.

In a homogeneous system with a constant concentration of the initial reactants A_0 and B_0, Eqs. (2) admit the homogeneous steady state (SS) $(X_{SS}, Y_{SS}) = (A_0, B_0/A_0)$. If B_0 is chosen as the bifurcation parameter, this SS becomes unstable towards a Hopf instability if $B_0 > B_c^H = 1 + A_0^2$ evolving then into a homogeneous limit cycle characterized by a critical frequency $\omega = iA_0$. In the presence of differential diffusion (namely, the activator X diffusing slower than the inhibitor Y), this SS becomes unstable toward a Turing instability when

$$B_0 > B_c^T = (1 + A_0\sqrt{\delta})^2, \tag{3}$$

where $\delta = D_X/D_Y$. A stationary spatial pattern then emerges, characterized by an intrinsic wavelength

$$\lambda_T^* = 2\pi \frac{(D_X D_Y)^{1/4}}{A_0^{1/2}}. \tag{4}$$

The nature of the emerging Turing patterns depends on the value of the parameter B_0. In particular, spots distributed with a hexagonal symmetry are the first structures to appear close to the bifurcation point, followed by stripes when B_0 is increased above B_c^T [18,25]. Contrary to the case of phyllotactic Turing patterns slaved to a chemical front controlled by a gradient of A [17], here we consider homogeneous and constant distributions of A and B in a horizontal squared spatial domain of side $L_x = L_y = L$ in the (x, y) reference system. For all simulations, we take $A_0 = 2, B_0 = 3, \delta = 10$ such that supercritical conditions $(B_0 > B_c^T)$ for Turing spots are satisfied. The concentrations of the intermediates X and Y are initially set uniformly throughout space to their steady-state values $[X_{SS} = A_0, Y_{SS} = B_0/A_0, \forall (x, y)$ at $t = 0]$. The instability is then triggered by seeding the concentration of Y with additional white noise of amplitude equal to 1% of Y_{SS} within a circular area of radius λ_T^* around the center $(L/2, L/2)$ of the spatial domain. The reaction-diffusion equations (2) are solved using the Alternating Direction Implicit method (ADI) [26], with spatial integration steps $h_x = h_y = 0.5$ and the time step $h_t = 0.001$. These values were first tested to ensure convergent numerical solutions. No-flux boundary conditions are imposed for all species at the reactor boundaries. The resulting patterns were found to be largely insensitive to the choice of boundary conditions, as confirmed by additional simulations with fixed (Dirichlet) boundary conditions.

B. Phyllotactic Turing patterns

Figure 1 shows the typical spatiotemporal development of the Turing instability guided by the radial growth of a central perturbation. A Turing front propagates through the unstable medium with constant speed from the nucleation area, separating the homogeneous unstable steady state region ahead from stationary Turing structures behind it. These concentric rings follow the same dynamical properties as the related one-dimensional case [27]. For the parameter values selected, concentric metastable rings first form. Later, they undergo a secondary transverse breaking of symmetry, progressively decomposing into spots. The decomposition of metastable stripes into spots starts initially at the reactor center, following the radially expanding pattern. However, it also develops backward from the reactor borders once the stripes touch the edges of the spatial domain, which act as additional nucleation points. Interestingly, as front- and back-growing spotted areas meet, they recombine and merge into a coherent global pattern, as if it were prescribed independently of the growth direction. The final pattern shows a morphology reminiscent of phyllotactic patterns, with spots arranged along spiral-shaped symmetric structures (parastichies). In time, these patterns progressively lose memory of the underlying radial geometry and reorganize to pave the available space with a regular hexagonal lattice.

C. Turing pattern analysis

We studied the properties of these phyllotacticlike Turing patterns by changing the related wavelength, which could possibly reflect on the angular properties of the resulting structures. To do so, we performed simulations at fixed

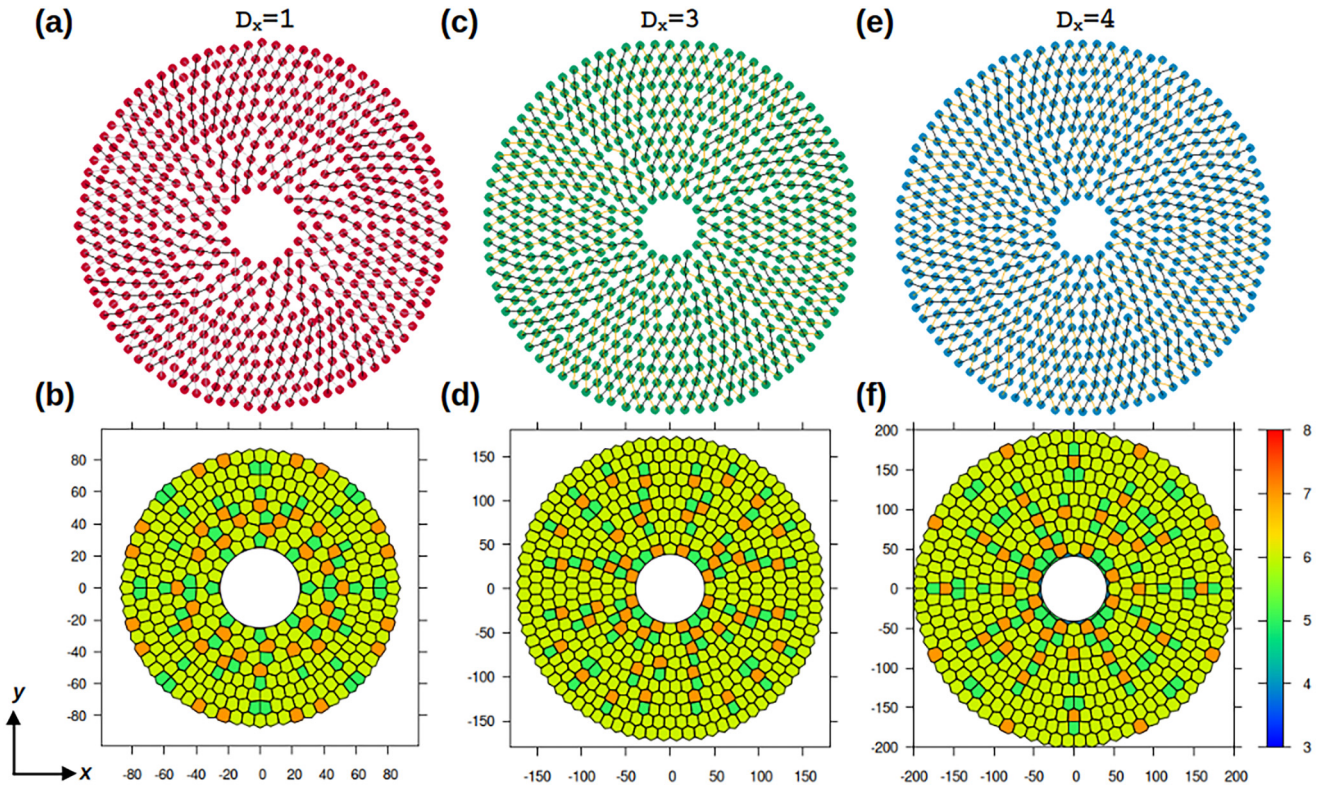

FIG. 2. Turing patterns obtained in the Brusselator with (a), (b) $D_X = 1$; (c), (d) $D_X = 3$; and (e), (f) $D_X = 4$ for $A_0 = 2$, $B_0 = 3$, $\delta = 10$, $L \approx 27\,\lambda_T^*$. Top panels show the distributions of spots, along with the underlying clockwise (black) and counterclockwise (orange) parastichies that connect the points toward the periphery of the reactor. Bottom panels illustrate the corresponding Voronoi diagrams obtained from the set of coordinates of the spots. Green, yellow, and orange cells present 5, 6, and 7 edges, respectively.

$A_0 = 2, B_0 = 3$ while varying the values of D_X and D_Y, keeping their ratio fixed ($\delta = 10$). This allows us to modify the wavelength λ_T^* given by Eq. (4) without changing the instability threshold B_c^T. Moreover, to have comparable results, we scaled the spatial domain size to that wavelength, such that $L \approx 27\lambda_T^*$.

In our exploration, we take $D_X \in [0.1, 5.0]$. For the sake of discussion, we illustrate in Fig. 2 only the representative cases $D_X = 1$ [Figs. 2(a) and 2(b)], 3 [Figs. 2(c) and 2(d)], and 4 [Figs. 2(e) and 2(f)]. The top panels show the distributions of spots, along with the underlying clockwise and counterclockwise parastichies that connect the points toward the periphery of the reactor. The bottom panels feature the corresponding Voronoi diagrams obtained from the set of coordinates of the spots. We can qualitatively appreciate that phyllotacticlike patterns are maintained while increasing the characteristic wavelength, without any change in the general morphology among the three cases. As seen in Fig. 3(a), each pattern is characterized by a dominant numerical wavelength λ_T, computed here as the most probable value of the distribution of the nearest-neighbor distance among spots. This numerical wavelength is close to the theoretical value, λ_T^*, given by relation Eq. (4) and indicated with dashed lines in the plot. This points to the fact that the distance between the spots is the one predicted by the linear stability analysis of Eqs. (2) also in this radial configuration.

The results of the analysis shown in Fig. 3 indicate that all simulations with varying D_X and D_Y can be reduced to the same scheme when rescaled by the inherent λ_T^* values. First, all the patterns present a similar number of parastichies, characterized by a high symmetry, i.e., the same number of clock- and counterclockwise spirals (n_s, n_s) with $n_s \sim 80$. The spirals were identified and drawn by connecting the nearest-neighbor spots on consecutive rings, separated by the smallest angular shift $|\Delta\phi|$ in the clockwise and counterclockwise directions. These angles were computed for all consecutive points along the spirals, and the dominant angular scale ruling the global morphology of the patterns was extracted as the most probable value of the resulting distributions. Figure 3(b) shows that all patterns are characterized by even distributions of $\Delta\phi$, with a mirroring symmetry with respect to the vertical axis at $\Delta\phi = 0$. This is due to the high symmetry of the patterns, which have the same number of oppositely oriented spirals with the same shift angle. The three distributions show almost overlapping profiles and peak values, the latter localized at small angles, $|\Delta\phi| \in [0.035, 0.045]$ rad (i.e., $2.25^\circ \pm 0.2^\circ$).

Second, the three patterns have a similar number of spots. To characterize this aspect, we indexed the spots by sorting their radial and angular positions in ascending order. We plot in Fig. 3(c) the radial position of the spots scaled by λ_T of each pattern as a function of the spot index. The resulting curves show a staircase profile that reflects the arrangement of the spots in successive concentric rings: each step corresponds to the kth ring with an almost fixed radius, r. All profiles collapse on the same trend, showing overlapping steps with a similar number of circles and spots per circle, as well as the

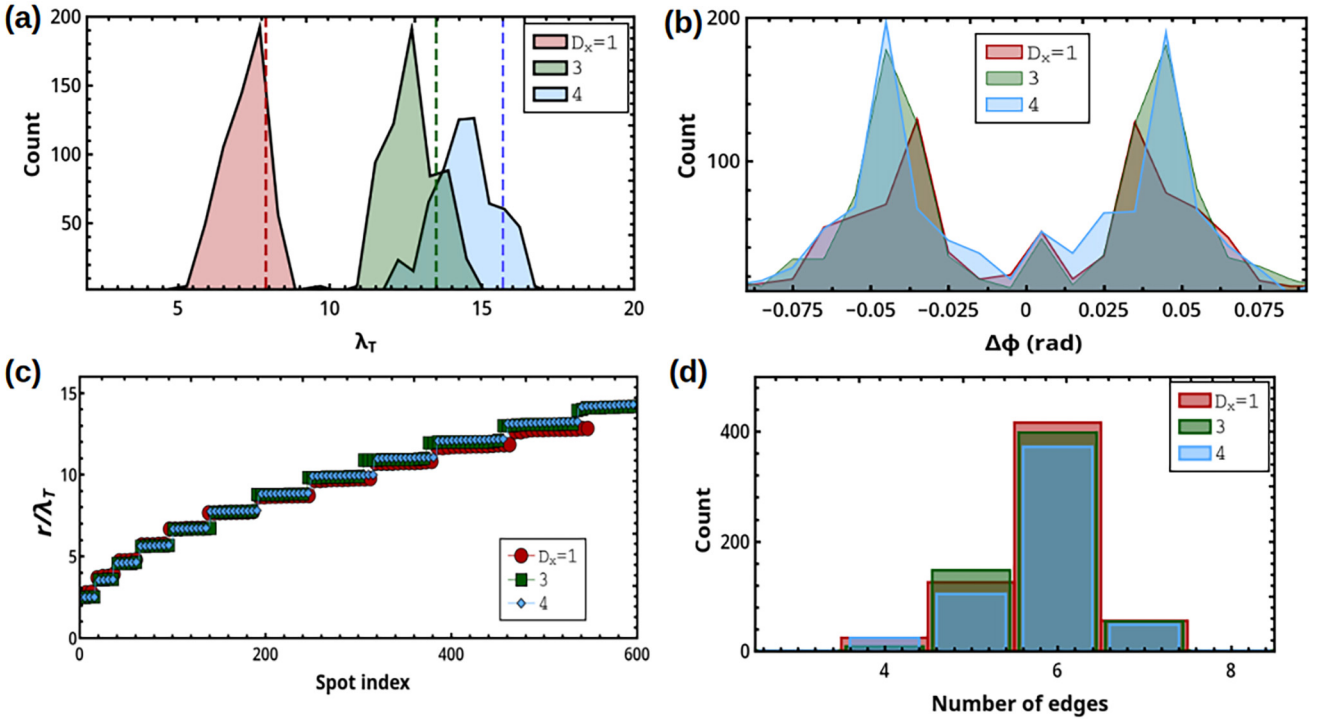

FIG. 3. Analysis of the Turing patterns illustrated in Fig. 2. (a) Characteristic numerical wavelength, λ_T obtained from the distribution of the nearest-neighbor distance. The vertical dashed lines represent the theoretical values λ_T^* given by Eq. (4). (b) Distribution of the smallest angular shift, $|\Delta\phi|$, separating consecutive points along the spirals in the clockwise and counterclockwise directions. (c) Radial position of the spots scaled by λ_T as a function of the spot index. (d) Statistics on the Voronoi cells with different number of edges.

same radial position of the circles in the rescaled coordinates. The combined radial and angular information indicates that all patterns are self-similar and rely on a common geometrical scheme.

Further information about the structure and the growth mechanism of this class of phyllotactic Turing patterns was obtained from the Voronoi diagrams [Figs. 2(b), 2(d), and 2(f)], which partition the plane into polygonal cells, each cell consisting of all points in the plane that are closer to a given site (generator point) than to any other site. Voronoi tessellations were computed using Qhull [28], a widely used computational geometry library that implements efficient algorithms for the construction of Voronoi diagrams and Delaunay triangulations from a set of Cartesian coordinates (in our case, the spots coordinates). The Voronoi analysis applied to the three cases here indicates that, far enough from the initial perturbation area (reactor center), the space is mainly partitioned into hexagonal cells, and the spots are thus mostly arranged on a hexagonal lattice adapted to the radial geometry. This imposes small distortions from regular hexagons and introduces compensatory pentagonal and heptagonal cells that fill void spaces. The statistics on the number of different cells are given in Fig. 3(d), where the distributions of the three cases are seen to overlap, and the leading contribution of the hexagonal cells can be appreciated.

As a whole, this picture indicates that our phyllotacticlike patterns, growing radially from a Turing instability in supercritical conditions, form from a spot packing mechanism that optimizes the covering of the available space [8]. Consistently with what is expected in that case, the number of left- and right-turning spirals is the same.

Inspired by Ref. [19], we substantiated this view by representing these self-similar patterns as a tiling of rigid disks with a radius λ_T/r in the rescaled space $(\phi,\ \rho)$. Here, $\phi \in [0, 2\pi]$ is the angular position of each spot along the rings and $\rho = \ln(r/r_0) \in [0, \ln(r_{\max}/r_0)]$, where r_0 and $r_{\max}$ are the radial distances of the first and last rings, respectively. The variable ρ is a scaled radial coordinate that compensates for the decrease in the disk radius, maintaining the rings mutually adjacent.

In the plot shown in Fig. 4(a), each horizontal array of disks corresponds to a ring of the radial patterns, indicated by index k, and more specifically, to a front (i.e., the set of elements with the sufficient information needed to introduce new elements, i.e., the spots of the next ring [19]). The first array with eight disks represents the ring $k = 0$ for $r = r_0$ (not shown in the patterns illustrated in the top panels of Fig. 2) while $k = 1$ $(r = r_1)$ corresponds to the first ring visible in Fig. 2. The structure grows by maximizing the minimal distance among the disks of consecutive rings, with new elements accommodating themselves in the interstitial regions left by previous disks. In this framework, the spirals connecting the closest disks in successive rings in the physical space follow tilted lines characterized by an almost constant slope. The resulting triangular packing is characterized by an elementary cell with three vectors, one corresponding to the angular coordinate and two (equivalent, with opposite directions) oriented along the direction where clockwise and counterclockwise spirals

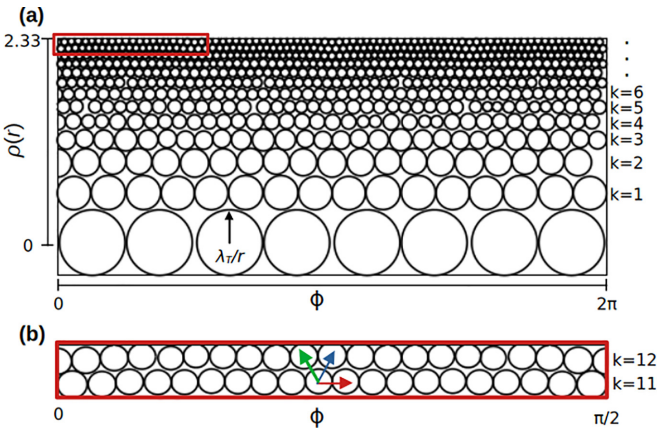

FIG. 4. (a) Representation of a Turing self-similar pattern [see, for instance, Fig. 2(c)] as a tiling of rigid disks of radius λ_T/r in the rescaled space (ϕ, ρ), where $\phi \in [0, 2\pi]$ is the angular position of each spot along the rings and $\rho = \ln(r/r_0) \in [0, \ln(r_{\max}/r_0)]$ (r_0 and $r_{\max}$ are the radial distance of the first and the last ring, respectively) is the rescaled radial position. The first array with eight disks corresponds to ring $k = 0$ for $r = r_0$ (not shown in the patterns of Fig. 2), while the second array with 16 disks describes ring $k = 1$ for $r = r_1$. (b) Detail of the plot for $k = 11$, 12 and $\phi \in [0, \pi/2]$. The primitive vectors of the triangular lattice characterizing the pattern are shown.

grow [see the example of the red, blue, and green vectors in Fig. 4(b) for the arrays $k = 10$ and 11]. The constitutive vectors have the same magnitude ($\approx 1/k$) and are separated by an angle $\approx \pi/3$.

This lattice of spot centers is the dual description of the hexagonal tessellation of space in the Voronoi diagram above and, thus, is at the origin of the symmetry of the pattern with the same number of oppositely oriented spirals. The geometrical constraint imposed by the triangular packing suggests that the angular shift between the closest neighbors in successive rings scales as $\Delta\phi \sim 1/(2k)$, i.e., half the magnitude of the horizontal cell vector of the kth level. Figure 5(a) shows that the values of the angular shift computed from simulation data in the (ϕ, ρ) space converge to this trend as soon as $k > 3$. For example, when $k = 12$, $\Delta\phi \sim 1/24 \sim 0.04$, which agrees with the analysis reported above in Fig. 3(b) for these patterns. As k increases, $\Delta\phi$ decreases slowly, which justifies the apparent convergence to an asymptotic limit. Figure 5(b) shows that successive arrays are separated by $\Delta\rho = \ln(r_k/r_{k-1})$ which, since $r_k - r_0 \approx \lambda_T\, k$, can be rewritten as $\ln(k/(k-1)) \to 1/k$ when $k \gg 1$. This explains the almost constant slope of the lines representing the spirals in the (ϕ, ρ) space, $\Delta\phi/\Delta\rho \to 1/2$ as k increases [Fig. 5(c)].

Finally, according to the framework introduced by Golé *et al.* [19], the number n_s of visible spirals in a phyllotactic pattern can be controlled by the dimensionless parameter

$$\Gamma = \frac{\lambda}{2\pi r} \sim \frac{1}{n_s}, \tag{5}$$

where λ generically indicates the characteristic wavelength of the pattern and r is the radial distance at which new spots or primordia appear. The intersection of $\Gamma(r)$ with $1/n_s$ gives the radius r at which n_s spirals will be visible in the pattern.

In our previous study [17], we investigated the patterns generated by a Turing instability expanding radially as a stable stationary structure behind a reaction-diffusion or a reaction-diffusion-advection front controlled by a gradient of the control parameter A (one of the Brusselator reactants). In that scenario, the characteristic wavelength $\lambda \sim A$ of the

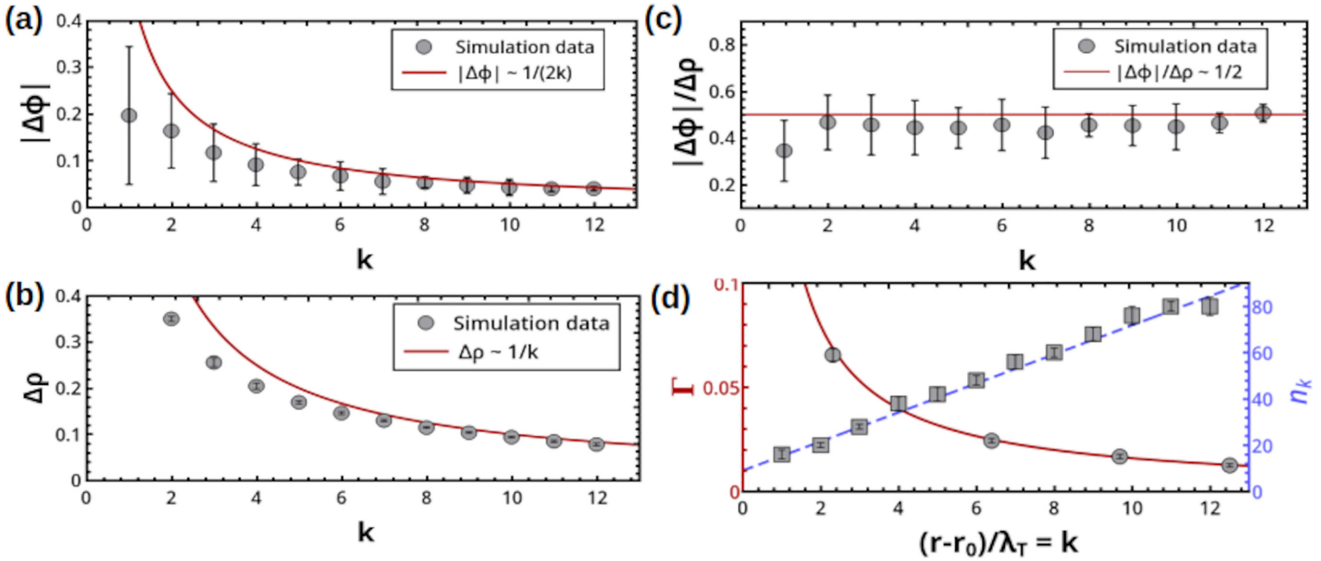

FIG. 5. Characterization of the Turing tiling of Fig. 4. (a) Angular shift $\Delta\phi$ between the closest neighbors in successive arrays scaling with the kth ring as $\Delta\phi \sim 1/(2k)$. (b) Radial distance between closest spots in successive arrays, scaling as $\Delta\rho = 1/k$. (c) Slope of the lines representing the spirals in the (ϕ, ρ) space, $\Delta\phi/\Delta\rho \to 1/2$ as k increases. (d) Comparison between the expected value of $\Gamma = 1/(2\pi k)$ (red solid curve) and the same observable obtained from simulation data as $1/n_s$, where n_s is the number of spirals. This also corresponds to $1/n_{k-1}$, where n_k is the number of spots in the kth ring (gray squares to be compared with the theoretical trend $n_k \approx n_0 + 2\pi k$ indicated with blue dashed line).

pattern increased linearly with r and, hence, Γ was constant, implying that the number of spirals was also maintained constant in the course of the patterns development. By contrast, here A is constant; hence λ remains constant, and thus Γ decreases with r, corresponding to an increase in the number of spirals during the pattern growth from the center to the periphery. This can be seen in Figs. 2(a)–2(c), where new spirals and defects appear when moving away from the center. To quantify this trend, we calculated the number of spirals at successive distances for each pattern and compared the resulting value $(1/n_s(r))$ with the theoretical profile $\Gamma = \lambda/(2\pi r)$, expressed as a function of $(r - r_0)/\lambda_T = k$. Figure 5(d) shows that the data obtained from the numerical simulations (circles) are in excellent agreement with the theory (red solid curve). We can see that in our case the parameter Γ also corresponds to the reciprocal of the number of spots n_k in the kth ring. This number increases discretely with the formation of new rings as

$$n_k \approx n_0 + \lfloor 2\pi k \rfloor, \tag{6}$$

where $n_0 \approx \lfloor 2\pi r_0/\lambda_T \rfloor$ is the number of disks on the initial ring at r_0. The actual number of spots per ring obtained from simulation data is reported with squares in Fig. 5(d) and obeys this trend (blue dotted line), with some deviations as the pattern expands. We can then rewrite Γ as

$$\Gamma = \frac{\lambda_T}{2\pi(r_k - r_0)} \sim \frac{1}{n_k} \sim \frac{1}{2\pi k}, \tag{7}$$

Comparison of Eq. (5) with Eq. (7) indicates that the number of spirals n_s visible at a given extent of these patterns is imposed by the number of spots n_{k-1} on the previous ring. This is confirmed by the analysis of numerical data and is physically consistent with the fact that any spot in the ring at the rim of the pattern can be either the end of a previous spiral or the primordium of a new one. The number of spirals at a given radius r_k corresponds to the number of spots in the $(k-1)$th ring, n_{k-1}, and not exactly to n_k because at least two consecutive spots are needed to define a spiral.

III. PHASE SEPARATION SPOTS

The mechanism driving the emergence of phyllotacticlike patterns behind a perturbation propagating in an unstable steady state can also be evidenced by a thermodynamic instability such as spinodal decomposition, which can provide a source of transverse symmetry breaking (spots). To explore this possibility, we use the CH model [29], widely used to study periodic pattern formation during phase separation, with applications in diblock copolymer segregation, multiphase fluid flows, microstructures with elastic inhomogeneity, and tumor growth simulation, to name a few [30,31]. Among others, the CH model of spinodal decomposition has been successfully adapted to simulate the formation of spiraled patterns driven by an $A + B \rightarrow C$ precipitation reaction [17] and the formation of Liesegang structures [32–34]. Here, we consider the system in initial supercritical homogeneous conditions and analyze the pavement of the plane by spot patterns growing radially following a localized perturbation.

A. Cahn-Hilliard model

A radially growing phase separation process guided by a perturbative front can be described by the CH equation

$$\partial_t \xi = -D\,\nabla^2(\epsilon\xi - \gamma\xi^3 + \sigma\nabla^2\xi), \tag{8}$$

where ξ is a phase variable. The parameters ϵ and γ are two positive constants that set the boundary between the stable and metastable regions ($\xi_m = \pm\sqrt{\epsilon/\gamma}$), and the spinodal line between the metastable and unstable regions ($\xi_s = \pm\sqrt{\epsilon/3\gamma}$). If the initial conditions are spatially set in supercritical conditions, i.e., $\xi_0(x, y) \in [\pm\sqrt{\epsilon/3\gamma}]$, perturbations will grow and drive a phase separation between regions of high-valued ($\xi = \sqrt{\epsilon/\gamma}$) and low-valued ($\xi = -\sqrt{\epsilon/\gamma}$) areas in the form of bands or spots patterns. D is the mobility coefficient, while $\sigma \in [0, 1]$ describes the energy cost of creating an interface between the two phases. The characteristic wavelength of the pattern, derived from the linear stability analysis of Eq. (8), is equal to [17]

$$\lambda^*_{\mathrm{CH}} = 2\pi\sqrt{\frac{\sigma}{\left(\epsilon - 3\gamma\xi_0^2\right)}}. \tag{9}$$

Equation (9) shows that the characteristic wavelength results from a balance between the gradient-energy penalty, controlled by σ, and the local thermodynamic instability, quantified by $-f''(\xi_0) = \epsilon - 3\gamma\xi_0^2$, where $f(\xi_0) = -\frac{1}{2}\epsilon\xi_0^2 + \frac{1}{4}\gamma\xi_0^4$ is the local free-energy density. Increasing σ favors larger characteristic wavelengths, whereas increasing $|f''(\xi_0)|$ leads to shorter-wavelength instabilities. The ratio σ/D defines a characteristic timescale for the growth of unstable modes [35]. The Cahn-Hilliard model (8) has been used to describe a variety of precipitation patterns, ranging from regular bands to helices and spots [33–35]. More recently, it has been shown that when initiating the system in the stable steady state, a reaction front increasing the value of ξ can locally bring the system into the unstable region, and phase separation follows the evolution of the reactive front [17,32–34].

According to previous works [33], a transverse breaking of symmetry with spots can be obtained using $D = 1$, $\gamma = 0.2$, $\sigma = 0.1$, and $\epsilon = 1$ (implying $\xi_m \approx \pm 2.2$). In our simulations, we adopt this parameter setting and tune $\sigma \in [0.1, 2]$ to study the growth dynamics and morphology of the pattern while changing the characteristic wavelength. The system is initially set in supercritical conditions, $\xi_0(x, y) = -1$, over a squared spatial domain of size $L_x = L_y = L$, except within a circular area of radius $0.04 \times L$ centered in the middle of the spatial domain $(L/2, L/2)$, where $\xi_0(x, y) = -\sqrt{\epsilon/\gamma}$. This initiates the radial expansion of a perturbation front that sustains the progressive formation of the phase separation patterns. The CH model (8) is solved using the ADI method [26], using a uniform spatial grid with $h_x = h_y = 0.5$ and a time step $h_t = 0.001$. These values were tested to ensure numerically stable and sufficiently resolved solutions. Unlike the Brusselator model, the CH equation is known to exhibit sensitivity to initial conditions and numerical noise, which can lead to differences in the detailed morphology of the patterns upon spatial grid refinement [17]. In our simulations, we verified that the main geometrical features of the patterns are preserved upon grid refinement. No-flux boundary

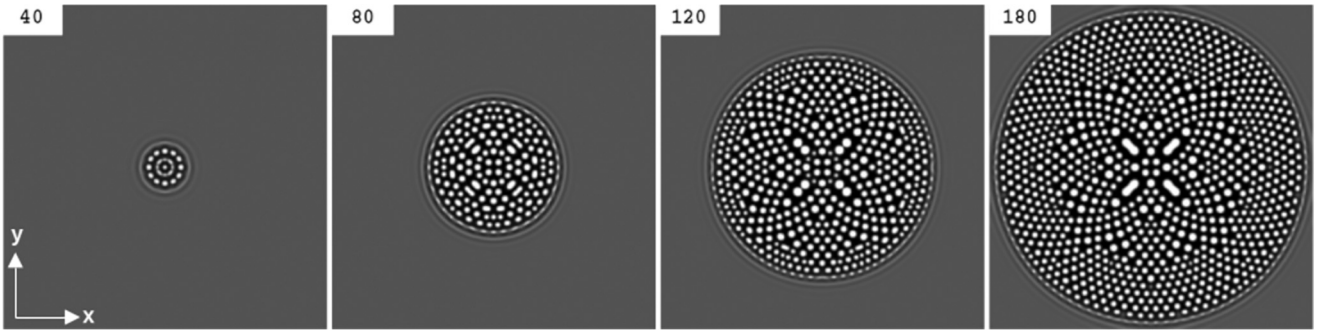

FIG. 6. Spatiotemporal evolution of the phase field $\xi(x, y)$ obtained by solving the CH model (8) with $\xi_0(x, y) = -1$, $D = 1$, $\gamma = 0.2$, $\sigma = 0.2$, $\epsilon = 1$, $L = 250$. The dimensionless time is given in the upper left corner.

conditions are imposed at the reactor boundaries. The resulting patterns are largely insensitive to the choice of boundary conditions, as confirmed by additional simulations with fixed (Dirichlet) boundary conditions, which produce analogous patterns.

B. Phyllotactic phase separation

Figure 6 shows the typical spatiotemporal development of the phase separation instability initiated and guided by the radial growth of a central perturbation. The instability front propagates from the center towards the borders, inducing a progressive and instantaneous phase separation in the form of discrete and consecutive rings, which successively decompose into spots with an approximately fixed wavelength. Similarly to the patterns obtained above with the Turing instability, the structure grows by successive rings, which then undergo a transverse breaking of symmetry to form spots arranged in a phyllotacticlike morphology. However, in this case, the decomposition of metastable rings into spots follows the radial evolution of the pattern, i.e., it occurs only in the outward direction. Some coalescence can be observed, particularly near the central region where the instability is triggered. During the course of time, spots agglomerate with their closest neighbors, which introduces some vacancies and larger spots, visually enhancing the phyllotactic nature of the final structures. Long-time coarsening is a well known phenomenon in Cahn-Hilliard dynamics [31,36].

Unlike the case where the growth of the instability is governed by an $A + B \to C$ reaction front [17], in which the radial evolution of the pattern rim obeys a diffusive $t^{1/2}$ scaling, here the structure expands linearly in time, following the speed of the perturbation propagation.

C. Cahn-Hilliard pattern analysis

Following the analysis performed for the Turing case, we check the robustness of the phyllotacticlike ordering obtained with the supercritical Cahn-Hilliard model and characterize the pattern properties when varying the characteristic wavelength by tuning $\sigma \in [0.1, 2]$. To have comparable results, we scale the size of the spatial simulation domain according to the wavelength of the system, such that $L \sim 50\,\lambda^*_{\mathrm{CH}}$. The representative cases illustrated in Fig. 7 show (i) the distributions of spots and underlying spirals and (ii) the related Voronoi diagrams. The statistical description of the pattern properties is given in Fig. 8. Altogether, the analysis reveals that these phase separation patterns share the same features as those obtained from the Turing instability.

First, the structures are characterized by a dominant wavelength that scales as the theoretical value [Eq. (9)] predicted by the linear stability analysis, i.e., it increases linearly with $\sqrt{\sigma}$ [Fig. 8(a)]. Scaled by this intrinsic length, the patterns show self-similar properties. In particular, all patterns present a similar number of parastichies, characterized by high symmetry, i.e., the same number of clockwise and counterclockwise spirals (n_s, n_s), with $n_s \sim 80$ for a pattern extent of $k = 13$ rings. The three distributions describing the shift angle of the spirals [Fig. 8(b)] show overlapping profiles for the three cases and comparable peak values localized at small angles, $|\phi| \in [0.035, 0.045]$ rad (i.e., $\approx 2.25 \pm 0.2^\circ$, pretty similar to the Turing case). Moreover, by sorting the spots by their radial and angular values in ascending order, the spot positions, scaled by λ_{CH} as a function of the spot indexes, collapse to the same evolution for the three patterns under consideration [Fig. 8(c)]. The Voronoi diagrams and related statistics in Fig. 8(d) show that, far enough from the perturbation area where coalescence is more impactful, the space is mainly partitioned into hexagonal cells, and the spots are thus mostly arranged on a hexagonal lattice compatible with a spot packing growth mechanism. This justifies an even number of left- and right-turning spirals also in this case. Following the analysis carried out for the Turing scenario, we characterize these self-similar patterns (rescaled by the intrinsic wavelength) in the polar coordinates (ϕ, ρ) (Fig. 9). Again, the structure grows by maximizing the minimal distance among the disks of the consecutive rings and new disks occupying the interstitial regions left by previous disks. In this resulting triangular packing, we find that the angular shift between the closest neighbors in successive rings scales as $\Delta\phi \sim 1/(2k)$ as soon as $k > 2$ [see Fig. 10(a)]. However, instead of the scaling $\Delta\rho \sim 1/k$ obtained in the Turing scenario, we find $\Delta\rho \sim 1/(1.3k)$, which is the best fit of the simulation data in Fig. 10(b). As expected, a good fit between the simulation data and the predicted trend can only be found for large values of k, while there is an important discrepancy for low values of k. The scalings of $\Delta\phi$ and $\Delta\rho$ explain the different slopes of the lines representing the spirals in the (ϕ, ρ) space for the CH patterns with respect to the Turing case. Here $\Delta\phi/\Delta\rho$ converges to $1.3/2 \approx 0.65$ as k increases [Fig. 10(c)], differently

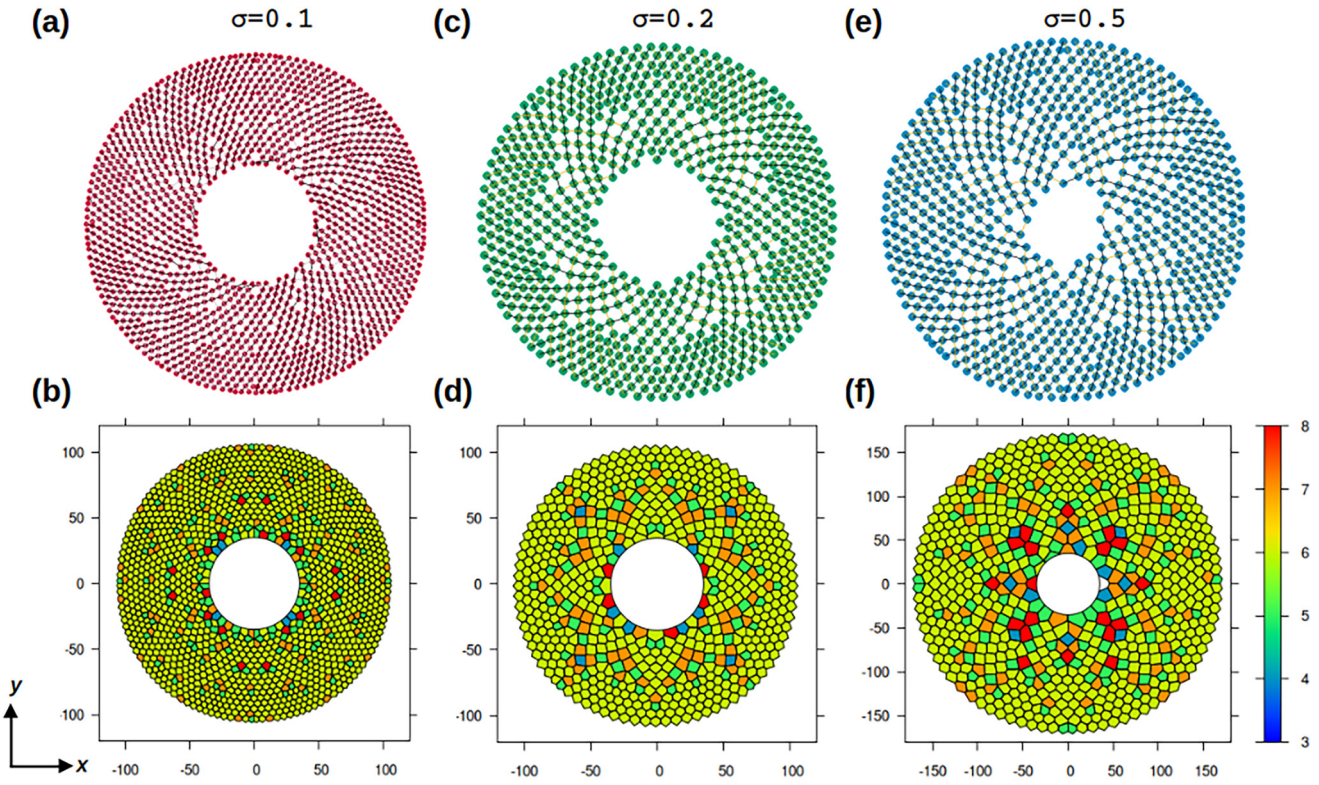

FIG. 7. Characterization of the Cahn-Hilliard patterns obtained for (a), (b) $\sigma = 0.1$; (c), (d) $\sigma = 0.2$; and (e), (f) $\sigma = 0.5$ for $\xi_0(x, y) = -1$, $D = 1$, $\gamma = 0.2$, $\epsilon = 1$, $L \approx 50\,\lambda^*_{\mathrm{CH}}$. Top panels show the distributions of spots, along with the underlying clockwise (black) and counterclockwise (orange) spirals that connect the points toward the periphery of the reactor. Bottom panels illustrate the corresponding Voronoi diagrams obtained from the set of coordinates of the spots. Green, yellow, orange, and red cells present 5, 6, 7, and 8 edges, respectively.

from Turing patterns where $\Delta\phi/\Delta\rho \to 1/2$. This quantity, measuring the divergence of the pattern from a growth parallel to the radial coordinate, justifies why the phyllotactic morphology of CH structures appears more striking compared to the Turing case.

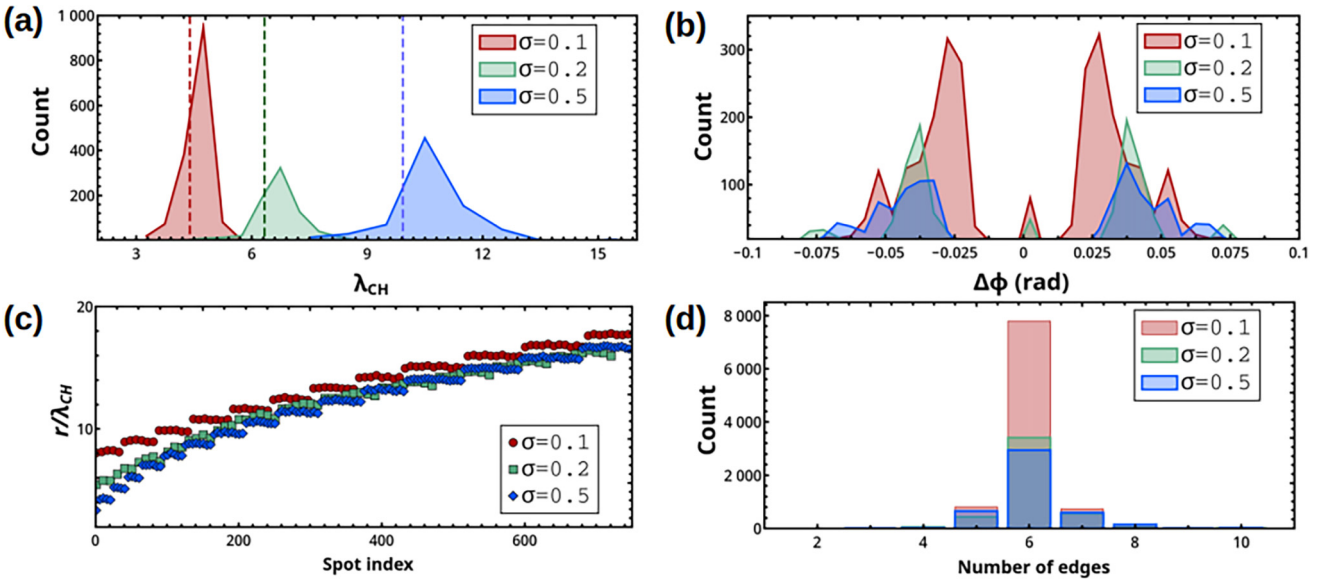

FIG. 8. Analysis of the Cahn-Hilliard patterns illustrated in Fig. 7. (a) Characteristic numerical wavelength, λ_{CH} obtained from the distribution of the nearest-neighbor distance. The vertical dashed lines represent the theoretical values of λ^*_{CH} given by Eq. (9). (b) Distribution of the smallest angular shift, $|\Delta\phi|$, separating consecutive points along the spirals in the clockwise and counterclockwise directions. (c) Radial position of the spots scaled by λ_{CH} of each pattern as a function of the spot index. (d) Statistics of the Voronoi cells with different number of edges.

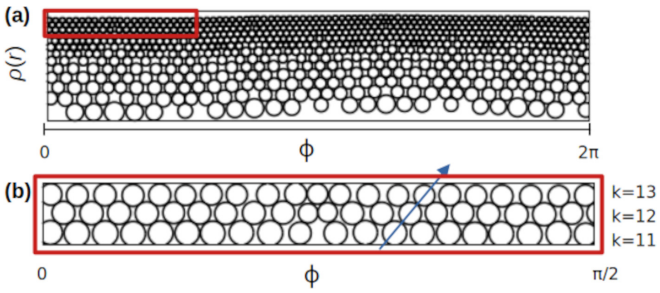

FIG. 9. (a) Representation of the self-similar Cahn-Hilliard patterns as a tiling of rigid disks of radius λ_{CH}/r in the rescaled space (ϕ, ρ). (b) Detail of the plot for $k = 11, 12, 13$, and $\phi \in [0, \pi/2]$; the arrow shows the constant slope $\Delta\phi/\Delta\rho$.

Importantly, the scaling of $\Delta\rho$ does not imply that the physical distance between successive rings decreases during growth. In particular, since $\Delta\rho \approx \Delta r/r$, the physical radial increment satisfies

$$\Delta r \sim \frac{1}{a}\frac{r_k - r_0}{k}, \tag{10}$$

where a is the scaling factor obtained from the fitting of $\Delta\rho(k)$ ($a = 1$ and 1.3 for the Turing and the CH case, respectively). This, combined with $r_k - r_0 \sim k\lambda$, gives

$$\Delta r \sim \frac{1}{a}\lambda. \tag{11}$$

This means that in both scenarios, Δr remains proportional to the characteristic length of the pattern, λ, and is asymptotically constant in spatial units. However, whereas in Turing patterns ($a = 1$) the radial separation between adjacent rings is comparable to the characteristic wavelength λ_T, in the Cahn–Hilliard case ($a = 1.3$) the inter-ring spacing falls below λ_{CH}. This radial compression results in a qualitatively different spatial organization, characterized by more tightly curled structures. Finally, we checked the dependence of the number n_s of visible spirals on the parameter

$$\Gamma = \frac{\lambda_{CH}}{2\pi r_k} \approx \frac{1}{n_s}, \tag{12}$$

which, like in the Turing case, here also decreases as the pattern grows, since λ_{CH} is constant. Figure 10(d) shows that the values of Γ, calculated as the reciprocal of the number of spirals at different radii, follow the expected trend

$$\Gamma \sim \frac{1}{n_k} \sim \frac{1}{2\pi k}. \tag{13}$$

In particular, the number of spirals at a given radius r_k corresponds to the number of spots in the $(k-1)$th ring, n_{k-1}, and not exactly n_k because at least two consecutive spots are needed to define a spiral. Some discrepancies with respect to the theoretical trend $(n_k)^{-1} \sim (2\pi k)^{-1}$ are due to the fact that the number of spots per ring fluctuates over the theoretical line $n_k \approx n_0 + 2\pi k$ [compare the squares and the blue dashed line in Fig. 10(d)], since the actual number of spots is affected by coalescence.

IV. CONCLUDING DISCUSSION

Phyllotactic structures are not only fascinating geometries but also a source of inspiration for technological applications, such as biomimetic solar panels designed to optimize energy absorption. Both their fundamental scientific significance and their potential practical impact make the investigation of the mechanisms underlying their formation particularly compelling.

The central idea of this work was to exploit spatial self-organizing processes capable of generating spotlike structures to construct phyllotacticlike patterns. In particular, building on previous studies, we investigated to what extent the radial growth of spatial symmetry-breaking instabilities characterized by an intrinsic wavelength can embody the minimal ingredients required for the spontaneous formation of phyllotactic structures, thereby enabling the formulation of a universal mechanism underlying their appearance. In contrast to our previous study, where the spatial development of the instability was sustained by a reactive front [17], here we explored the pattern evolution when the system is initially in supercritical conditions (i.e., uniformly unstable), and the propagation is driven by a perturbative front. We considered two conceptually distinct sources of spatial symmetry breaking: the Turing instability describing far-from-equilibrium self-organization and an equilibrium instability, namely, spinodal decomposition. The Brusselator and the Cahn–Hilliard models were employed to describe the first and second scenarios, respectively. In both systems, we find that phyllotactic patterning can be obtained when perturbations invade an unstable steady state radially.

Despite their different physical origins, the structures and dynamics obtained with the two models exhibit striking similarities. In both cases, phyllotactic patterns develop through the progressive formation of concentric ringlike structures followed by their fragmentation into spots. The resulting patterns display high symmetry, with equal numbers of oppositely oriented parastichies, a constant angular shift between successive spots along the spirals, and a dominant wavelength dictated by the linear stability properties of the system. The emergence of phyllotactic morphologies is found to be robust under variations of the characteristic wavelength. More precisely, patterns of different wavelengths are self-similar, converging to the same geometrical scheme once normalized by their intrinsic wavelength. Overall, the emergence of phyllotacticlike order is robust with respect to domain size, boundary conditions, and spatial discretization, although the Cahn–Hilliard model can exhibit some sensitivity of the detailed pattern morphology to grid refinement. The number of visible spirals in these self-similar patterns can be controlled by the dimensionless parameter Γ which, for these scenarios, corresponds to the inverse of the number of spots of the last rings of the pattern or, equivalently, to the inverse of the number of constitutive rings.

Within this framework, phyllotaxy arises from an intrinsic space-optimization mechanism ensured by maximized packing through a hexagonal arrangement of spots [8], as revealed by the corresponding Voronoi diagrams. Similarly to the spirals obtained in the wake of a reaction front [17], the phyllotactic patterns obtained here with both the Brusselator

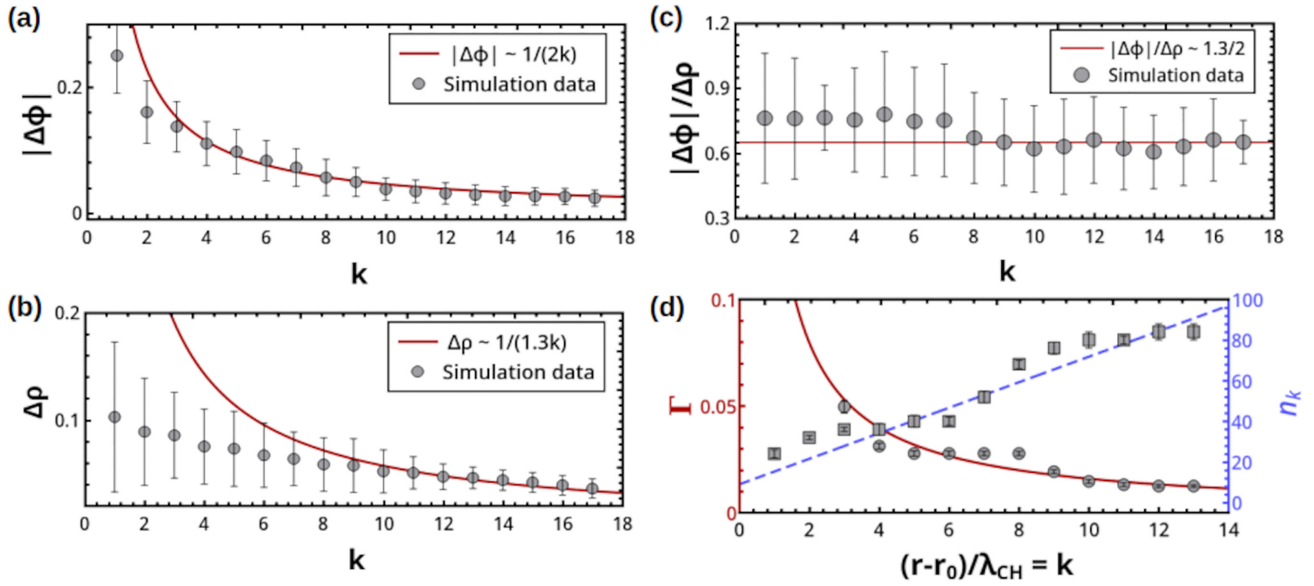

FIG. 10. Characterization of the Cahn-Hilliard patterns obtained in Fig. 9. (a) Angular shift between the closest neighbors in successive arrays, scaling with the kth ring as $\Delta\phi \sim 1/(2k)$. (b) Radial distance of closest spots between successive arrays, scaling as $\Delta\rho = 1/(1.3k)$. (c) Slope of the lines representing the spirals in the (ϕ, ρ) space, $\Delta\phi/\Delta\rho \to 1.3/2$ as k increases. (d) Comparison between the expected value of $\Gamma = 1/(2\pi k)$ (red solid curve) and the same observable obtained from simulation data as $1/n_s$, where n_s is the number of spirals. This also corresponds to $1/n_{k-1}$, where n_k is the number of spots in the kth ring (gray squares to be compared with the theoretical trend $n_k \approx n_0 + 2\pi k$ indicated with blue dashed line).

and the Cahn–Hilliard models in homogeneous supercritical conditions can be classified as whorled modes, characterized by high symmetry and an equal number of clockwise and counterclockwise parastichies.

Unlike former experiments with ferromagnetic droplets [9], here the divergence angle is not imposed in the generative mechanism but emerges spontaneously as a result of the annular growth, induced by the shift between consecutive rings, and constraints for optimal packing.

This interpretation was further supported by analyzing the pattern as a tiling of rigid disks of radius λ/r in a rectangular domain of the rescaled space (ϕ, ρ), where λ is the characteristic length of the instability, $\phi \in [0, 2\pi]$ denotes the angular coordinate, and $\rho = \ln(r/r_0) \in [0, \ln(r_{\max}/r_0)]$, with r_0 and $r_{\max}$ representing the radii of the first and last rings, respectively. Both models indicate that phyllotactic growth proceeds by maximizing the minimal distance between disks belonging to consecutive rings, with new disks accommodating into the interstitial regions left by previously formed ones. The resulting triangular packing corresponds to the dual representation of the hexagonal Voronoi tessellation. Nevertheless, this characterization reveals that Turing- and phase separation-induced patterns select different primitive vectors for radial advance. In particular, CH patterns present a higher $\Delta\phi/\Delta\rho$ value that makes their phyllotactic morphology more striking. This quantity measures the slope of the arrays of disks representing the parastichies in this plot and gives the divergence of these lines from the radial axis.

In conclusion, our results expand the number of possible pathways for inducing phyllotacticlike patterns through spatial symmetry-breaking instabilities featuring spots coupled to radial growth. One mechanism relies on the radial development of an instability driven by a reaction–transport front that locally creates conditions for pattern emergence [17]. Here, we showed that another option is the propagation of a perturbation in an initially homogeneous steady state, which is unstable with respect to a transverse symmetry breaking instability. In both scenarios, the essential ingredients for phyllotactic genesis are preserved: radial growth and a fixed intrinsic wavelength imposed by the instability. Several examples of phyllotacticlike ordering can be reviewed and interpreted within this framework [37,38] while new ones could be sought in the realm of material sciences [39,40], precipitation reactions [17], or optics [14,41], to name a few.

In perspective, it remains to understand whether and how it is possible to introduce an asymmetry in these patterns to induce forms obeying the Fibonacci series. Future work will focus on the experimental implementation of the perturbation-driven scenario. Particularly promising in this direction is the use of self-organizing chemical systems, like the Belousov-Zhabotinsky reaction, which can generate autonomously *in situ* spiral forms and dashed waves [42–45], and thus represent a good ground for the controlled growth of phyllotactic structures.

ACKNOWLEDGMENTS

A.D. thanks FRS-FNRS for financial support under the PDR programme “Phyllo”. Our collaboration has benefited from financial support of the European Space Agency.

DATA AVAILABILITY

There are no publicly available research data or software supporting this manuscript. Requests for further information or data should be sent to the authors.

[1] R. Reber, N. Schwarz, and P. Winkielman, Processing fluency and aesthetic pleasure: Is beauty in the perceiver's processing experience? Pers. Soc. Psychol. Rev. **8**, 364 (2004).

[2] A. M. Turing, The chemical basis of morphogenesis, Philos. Trans. R. Soc. Lond. B Biol. Sci. **237**, 37 (1952).

[3] G. Nicolis and I. Prigogine, *Self-Organization in Nonequilibrium Systems* (Wiley, New York, 1977).

[4] M. A. Budroni and F. Rossi, Transport-driven chemical oscillations: A review, Phys. Chem. Chem. Phys. **26**, 29185 (2024).

[5] R. V. Jean, *Phyllotaxis: A Systemic Study in Plant Morphogenesis* (Cambridge University Press, Cambridge, 1994).

[6] I. Adler, D. Barabe, and R. V. Jean, A history of the study of phyllotaxis, Ann. Bot. **80**, 231 (1997).

[7] G. J. Mitchison, Phyllotaxis and the Fibonacci series, Science **196**, 270 (1977).

[8] S. Douady and Y. Couder, Phyllotaxis as a dynamical self organizing process part II: The spontaneous formation of a periodicity and the coexistence of spiral and whorled patterns, J. Theor. Biol. **178**, 275 (1996).

[9] S. Douady and Y. Couder, Phyllotaxis as a physical self-organized growth process, Phys. Rev. Lett. **68**, 2098 (1992).

[10] F. J. Richards, Phyllotaxis: Its quantitative expression and relation to growth in the apex, Philos. Trans. R. Soc. Lond. B Biol. Sci. **235**, 509 (1951).

[11] L. S. Levitov, Phyllotaxis of flux lattices in layered superconductors, Phys. Rev. Lett. **66**, 224 (1991).

[12] C. Li, X. Zhang, and Z. Cao, Triangular and Fibonacci number patterns driven by stress on core/shell microstructures, Science **309**, 909 (2005).

[13] C. Nisoli, N. M. Gabor, P. E. Lammert, J. D. Maynard, and V. H. Crespi, Static and dynamical phyllotaxis in a magnetic cactus, Phys. Rev. Lett. **102**, 186103 (2009).

[14] F. Haudin and S. Residori, Golden spirals as phyllotactic arrangements of optical patterns, Phys. Rev. E **87**, 020901(R) (2013).

[15] H. N. Yoshikawa, C. Mathis, P. Maissa, G. Rousseaux, and S. Douady, Pattern formation in bubbles emerging periodically from a liquid free surface, Eur. Phys. J. E **33**, 11 (2010).

[16] M. Pennybacker and A. C. Newell, Phyllotaxis, pushed pattern-forming fronts, and optimal packing, Phys. Rev. Lett. **110**, 248104 (2013).

[17] G. Facchini, M. A. Budroni, G. Schuszter, F. Brau, and A. De Wit, Phyllotactic structures in radially growing spatial symmetry breaking systems, Phys. Rev. Lett. **135**, 018001 (2025).

[18] A. De Wit, Spatial patterns and spatiotemporal dynamics in chemical systems, Adv. Chem. Phys. **109**, 435 (1999).

[19] C. Golé, J. Dumais, and S. Douady, Fibonacci or quasi-symmetric phyllotaxis. Part I: why? Acta Soc. Bot. Pol. **85**, 3533 (2016).

[20] I. Prigogine and R. Lefever, Symmetry breaking instabilities in dissipative systems, J. Chem. Phys. **48**, 1695 (1968).

[21] R. Lefever, G. Nicolis, and P. Borckmans, The Brusselator: It does oscillate all the same, J. Chem. Soc. Faraday Trans. 1 **84**, 1013 (1988).

[22] A. N. Zaikin and A. M. Zhabotinsky, Concentration wave propagation in two-dimensional liquid-phase self-oscillating system, Nature (London) **225**, 535 (1970).

[23] M. A. Budroni and A. De Wit, Localized stationary and traveling reaction-diffusion patterns in a two-layer $A + B \rightarrow$ oscillator system, Phys. Rev. E **93**, 062207 (2016).

[24] M. A. Budroni and A. De Wit, Dissipative structures: From reaction-diffusion to chemo-hydrodynamic patterns, Chaos **27**, 104617 (2017).

[25] G. Dewel, P. Borckmans, A. De Wit, B. Rudovics, J.-J. Perraud, E. Dulos, J. Boissonade, and P. De Kepper, Pattern selection and localized structures in reaction-diffusion systems, Physica A **213**, 181 (1995).

[26] D. W. Peaceman and H. H. Rachford, The numerical solution of parabolic and elliptic differential equations, J. Soc. Ind. Appl. Math. **3**, 28 (1955).

[27] O. Jensen, V. O. Pannbacker, E. Mosekilde, G. Dewel, and P. Borckmans, Localized structures and front propagation in the Lengyel-Epstein model, Phys. Rev. E **50**, 736 (1994).

[28] C. B. Barber, D. P. Dobkin, and H. Huhdanpaa, The quickhull algorithm for convex hulls, ACM Trans. Math. Software **22**, 469 (1996).

[29] J. W. Cahn and J. E. Hilliard, Free energy of a nonuniform system. I. Interfacial free energy, J. Chem. Phys. **28**, 258 (1958).

[30] J. Kim, S. Lee, Y. Choi, S.-M. Lee, and D. Jeong, Basic principles and practical applications of the Cahn-Hilliard equation, Math. Probl. Eng. **2016**, 1 (2016).

[31] A. Onuki, *Phase Transition Dynamics* (Cambridge University Press, Cambridge, 2002).

[32] T. Antal, M. Droz, J. Magnin, and Z. Rácz, Formation of Liesegang patterns: A spinodal decomposition scenario, Phys. Rev. Lett. **83**, 2880 (1999).

[33] M. Dayeh, M. Ammar, and M. Al-Ghoul, Transition from rings to spots in a precipitation reaction–diffusion system, RSC Adv. **4**, 60034 (2014).

[34] P. Papp, B. Bohner, A. Tóth, and D. Horváth, Fine tuning of pattern selection in the cadmium–hydroxide-system, J. Chem. Phys. **152**, 094906 (2020).

[35] S. Thomas, I. Lagzi, F. Molnár Jr., and Z. Rácz, Probability of the emergence of helical precipitation patterns in the wake of reaction-diffusion fronts, Phys. Rev. Lett. **110**, 078303 (2013).

[36] R. V. Kohn and F. Otto, Upper bounds on coarsening rates, Commun. Math. Phys. **229**, 375 (2002).

[37] E. O. Budrene and H. C. Berg, Dynamics of formation of symmetrical patterns by chemotactic bacteria, Nature (London) **376**, 49 (1995).

[38] M. F. Staddon, Phyllotaxis in a Keller-Segel model, Phys. Rev. E **113**, 034407 (2026).

[39] B. A. Grzybowski, *Chemistry in Motion: Reaction-Diffusion Systems for Micro- and Nanotechnology* (John Wiley & Sons, Ltd., Chichester, UK, 2009).

[40] M. Casiulis, A. Shih, and S. Martiniani, Gyromorphs: A new class of functional disordered materials, Phys. Rev. Lett. **135**, 196101 (2025).

[41] M. Tlidi, P. Mandel, and R. Lefever, Localized structures and localized patterns in optical bistability, Phys. Rev. Lett. **73**, 640 (1994).

[42] K. Agladze and V. Krinsky, Flower patterns in a growing active chemical medium, J. Phys. Chem. A **101**, 2739 (1997).

[43] M. A. Budroni and F. Rossi, A novel mechanism for *in situ* nucleation of spirals controlled by the interplay between phase fronts and reaction–diffusion waves in an oscillatory medium, J. Phys. Chem. C **119**, 9411 (2015).

[44] V. K. Vanag and I. R. Epstein, Dash waves in a reaction-diffusion system, Phys. Rev. Lett. **90**, 098301 (2003).

[45] J. Gao and C. Gu, Super multi-armed and segmented spiral pattern in a reaction-diffusion model, IEEE Access **7**, 140391 (2019).